Programmable Potentials Choreograph Defects in a Colloidal Crystal Shell

Guolong Zhu,[1,2,3] Lijuan Gao,[2] Yuming Wang,[2] Tsvi Tlusty,[3,4] and Li-Tang Yan[2,*]
[1]School of Physics and Electronics, Hunan University, Changsha 410082, China
[2]State Key Laboratory of Chemical Engineering, Department of Chemical Engineering, Tsinghua University, Beijing 100084, China
[3]Center for Soft and Living Matter, Institute for Basic Science (IBS), Ulsan 44919, South Korea
[4]Departments of Physics and Chemistry, Ulsan National Institute of Science and Technology, Ulsan 44919, South Korea

(Received 9 August 2023; revised 6 November 2023; accepted 19 December 2023; published 23 January 2024)

Crystallization on spherical surfaces is obliged by topology to induce lattice defects. But controlling the organization of such defects remains a great challenge due to the long-range constraints of the curved geometry. Here, we report on DNA-coated colloids whose programmable interaction potentials can be used to regulate the arrangement of defects and even achieve perfect icosahedral order on a sphere. Combined simulations and theoretical analysis show how the potential can be tuned by changing the temperature, thereby controlling the number of defects. An explicit expression for the effective potential is derived, allowing us to distinguish the effects of entropic repulsion and enthalpic attraction. Altogether, the present findings provide insights into the physics of crystallization on curved spaces and may be used for designing desired crystal geometries.

DOI: 10.1103/PhysRevLett.132.048201

Introduction.—Programming and controlling the arrangement of interacting particles on curved manifolds is a fundamental physical problem with various applications in many-body systems, living and engineered alike, such as the arrangement of proteins that comprise the shells of spherical viruses [1,2], fullerene patterns of carbon atoms [3], and colloidal particles confined at fluid-fluid interfaces [4–10]. The topology of the curved manifolds sets strict global constraints on the existence of defects through Euler's theorem. An important example is the crystallization of a triangular lattice on a spherical shell. In this case, the topological charges of the defects q_i are the deviation of the coordination numbers c_i of the N vertices from the ideal sixfold symmetry, $q_i = 6 - c_i$. Euler's theorem implies that total charge is a topological invariant, $\sum_{i=1}^{N} q_i = 12$ [11,12]. Thus, at least 12 5-coordinated disclination defects are required to embed a triangular lattice on a sphere. When N is not too large, configurations with exactly 12 5-coordinated defects located at the vertices of an icosahedron are believed to be the ground state [13]. However, as the number of particles grows, typically beyond a threshold value $N_t \approx 360$, it has been demonstrated that the total energy can be further lowered by introducing additional tightly bound fivefold and sevenfold disclination pairs, namely dislocations [4,14–16]. These topological defects govern the phase diagram of curved lattices and their elastic and rheological properties [17,18]. Hence, rational design of such materials necessitates physical understanding of defect interactions under global topological constraints, which is not yet established, although diverse interaction potentials have been considered [19].

In addressing this problem, DNA-coated colloids (DNACCs), which are colloidal particles functionalized with complementary single-stranded DNA (ssDNA) sequences allowing colloids to bind selectively [20], may be particularly beneficial. In contrast to the general short- [21–24] and long-range interactions [25,26] between colloidal particles, the interactions between DNACCs can be precisely and finely tuned to be repulsive or attractive [10,27,28]. Although numerous topologically defined crystalline architectures have been realized in self-assembling systems of DNACCs [29–40], their two-dimensional (2D) crystallization on curved manifolds, such as spheres, has been much less explored [41]. With the aid of the programmable DNACC potential with specific and directional interactions, crystals with fewer defects and even controllable distribution of defects may be achieved on a sphere. However, how such effects govern crystallization in curved geometries remains an open and mostly unexplored question.

In this Letter, we combine numerical simulations and theoretical analysis to study the ordering and defects of DNACCs on the spherical surface. The result has three merits: (1) the distinct potential of DNACCs is shown to allow a robust method to realize programmable control of defects on a sphere, where the number of defects can be remarkably reduced, achieving even perfect icosahedral order. (2) In stark contrast to other general potentials, the unique shape of this potential, regulated by the temperature, is revealed to govern the stability of different defect configurations, in which the two sides of the potential well dominate the five and sevenfold defects, respectively. (3) The explicit form of the effective DNACC potential

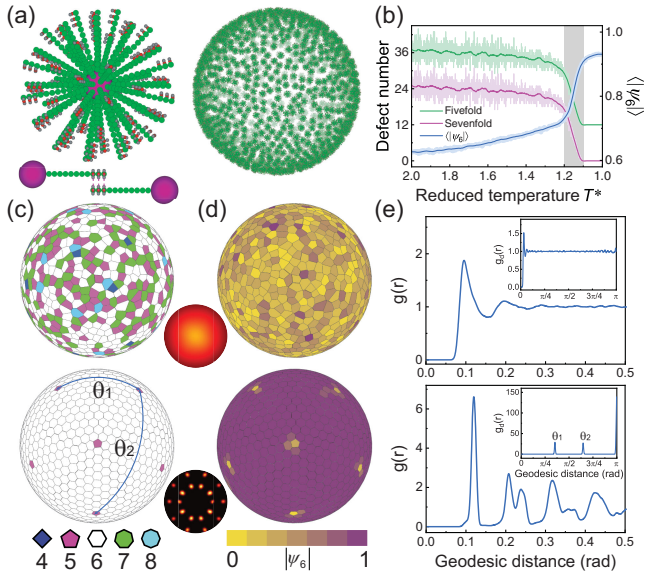

FIG. 1. (a) Schematic diagram illustrating the simulation model for crystallization of DNACCs on a sphere. (b) Defect number and average bond-orientation order parameter $\langle|\psi_6|\rangle$ during the annealing process. (c)–(e) Characterizations of the initial configuration (top) at $\eta = 0.6$, $T^* = 2.0$ and final configuration (bottom) at $\eta = 1.35$, $T^* = 1.0$. (c) Voronoi diagram showing lattice defects. Inset: diffraction pattern. (d) Bond-orientation order parameter $|\psi_6|$. (e) RDF of DNACCs $g(r)$. Inset: RDF of defects $g_d(r)$.

explains the physical origins of the entropic and enthalpic interactions, which may be useful for general theories of ordering and defects in curved spaces.

Simulation.—In this work, molecular dynamics (MD) simulations are employed to investigate the structural organizations of DNACCs confined on a spherical surface, as schemed in Fig. 1(a) [42]. Specifically, we use the coarse-grained flanking bead model, which has been extensively tested for robustly and reliably capturing the specific interactions between complementary bases [46–49]. The colloid is modeled as a spherical core with ssDNA chains distributed randomly on the surface and the chain number $f = 60$. The ssDNA are modeled as n_s spacer beads and n_l linker beads. Here, $n_s = 8$ and $n_l = 3$ represent the numbers of these different beads. Each linker bead has an additional structure, which includes a central bead mimicking the base-pairing interaction of nucleic acids and flanking beads protecting the central bead from binding to more than one complementary bead. The attractive interaction between central beads is modeled via the shifted Lennard-Jones potential with an interaction strength $\epsilon_0 = 6.0\epsilon$. ϵ is the unit of energy. DNACCs are confined in a shell through a strong shifted Lennard-Jones potential with $\epsilon_{\text{wall}} = 100\epsilon$ and particle dynamics are governed by the Langevin equation [50]. The reduced parameters used in this study are the area packing fraction $\eta = Nr_1^2/(4R^2)$ and the dimensionless temperature $T^* = k_B T/\epsilon$, where $N = 1002$ is the number of DNACCs, r_1 is the average distance between the center of a colloid and the ends of the relaxed DNA chains, R is the radius of the confining sphere, k_B is the Boltzmann constant, and T is the absolute temperature. To realize full crystallization, R is gradually reduced from a random initial configuration to $\eta = 1.35$, which is high enough for DNACC crystallization [51]. Then, thermal annealing is applied from $T^* = 2.0$ to $T^* = 1.0$ in 8×10^8 time steps to achieve active DNA hybridization.

We begin by examining the crystalline structures of DNACCs on the sphere. Voronoi tessellation of the surface shows that disclinations densely and randomly cover the initial configuration, while 12 isolated fivefold disclinations are located at the vertices of an icosahedron in the final configuration [Fig. 1(c)]. Similar patterns are exhibited by the 2D bond-orientational order parameter that measures the degree of hexagonal order: $\psi_6(\boldsymbol{r}_i) = (1/c_i)\sum_{j=1}^{c_i} e^{6k\theta_{ij}}$, where k is the imaginary unit and θ_{ij} is the angle between the line connecting particle i to its jth neighbor and an arbitrary reference axis [Fig. 1(d)]. Diffraction patterns further corroborate that the initial random configuration gives rise to a final configuration with icosahedral symmetry. To better understand the structural characteristics, the radial distribution function (RDF) between DNACCs and defects is calculated, demonstrating short-range ordering typical to liquids in the initial configuration but long-range ordering in the final configuration [Fig. 1(e)]. The reduction of defect number during annealing, accompanied by increasing values of $\langle|\psi_6|\rangle$, is presented in Fig. 1(b). There are only fivefold and sevenfold defects on the surface because these defect configurations lower the elastic energy on a sphere at high densities [14–16]. Moreover, the difference between the number of fivefold and sevenfold defects is always 12. Strikingly, an extreme change of defect number and $\langle|\psi_6|\rangle$ takes place at the same temperature around $T^* \approx 1.2$, after which there are exactly 12 fivefold defects on the sphere, corresponding to the perfect icosahedral order as indicated in the bottom panels of Figs. 1(c)–1(e). The physical origin of such a sharp transition will be elucidated in the following as well as the discussion section.

Next, we examine the defects during annealing. As shown in Fig. 2(a), the defects evolve into icosahedral order, a process accompanied by the elimination of the scars (lines of dislocations). Specifically, when two dislocations with opposite orientations merge by diffusion, they annihilate in pairs and reconfigure into regular hexagonal lattices, as denoted by red arrows and circles in Fig. 2(a). To further evaluate this temperature-induced transition from scars to isolated lattice defects, we trace the RDF of defects [Fig. 2(b)]. At $T^* = 2.0$, the scars tend to lie as far as possible from each other, and two slight peaks are observed in the RDF. As temperature is decreased, the peaks become sharper, indicating a more prominent

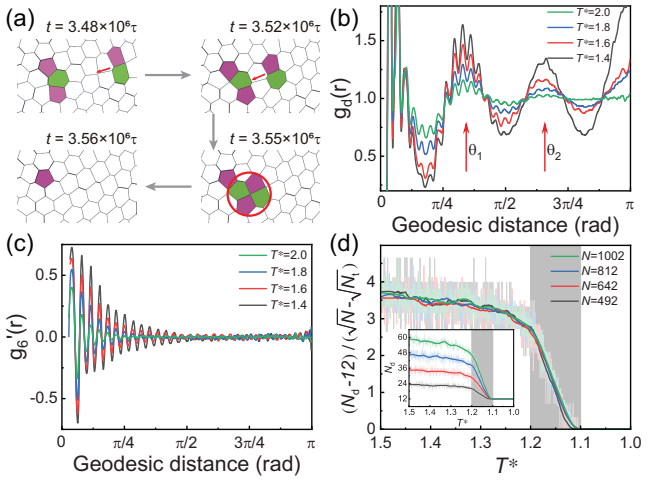

FIG. 2. (a) Snapshots demonstrating the elimination of dislocations. (b) RDFs of defects at different temperatures. (c) Orientational correlation functions $g_6'(r)$ of particles at different temperatures. (d) Temperature dependence of the normalized excess dislocations. Inset: total defect number as a function of temperature.

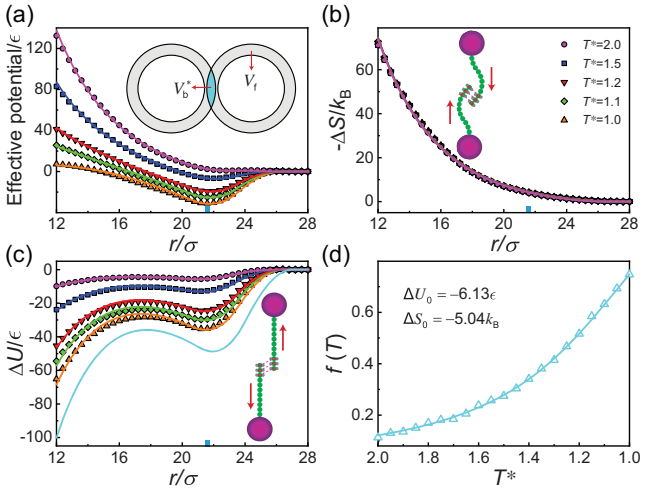

FIG. 3. (a) Effective potentials between DNACCs at different temperatures. Insets: representative schematic of the areas accessible to free (gray) and bound (cyan) sticky ends. (b) Entropic and (c) enthalpic contributions. Insets: schematic of conformational entropy penalty due to chain compression (b) and enthalpy gain from bond stretching (c). (d) Form factors at different temperatures. In (a)–(d), solid lines and symbols are theoretical and numerical results, respectively. In particular, the solid cyan line in (c) is the theoretical ΔU_t at $T = 0$. In (a)–(c), the same legend is presented in (b) and the short cyan bar on each horizontal axis indicates the bottom of the potential well.

transitional order with icosahedral symmetry on the sphere. To quantify the orientational order, we compute the orientational correlation function as follows:

$$g_6'(r) = \langle \psi_6'(\boldsymbol{r}_i)\psi_6'^*(\boldsymbol{r}_j)\rangle_{\arccos(\boldsymbol{r}_i\cdot\boldsymbol{r}_j/R^2)=r}, \tag{1}$$

where $\psi_6'(\boldsymbol{r})$ is the geodesic 2D bond-orientational order parameter [6]. The result indicates enhanced, long-range orientational order at lower temperatures as well [Fig. 2(c)].

To delineate the dramatic decrease in defect number at $T^* \approx 1.2$ in Fig. 1(b), the dependence of total defect number, N_d, on T for various values of R at $\eta = 1.35$ is examined. Indeed, the sharp fall of N_d occurs for all of R examined [Fig. 2(d)]. Furthermore, normalizing the excess dislocations $N_d - 12$ by $\sqrt{N} - \sqrt{N_t}$, which reflects the curvature, all the curves collapse onto a single master curve. The collapse indicates that the transition originates from physical principles linked to the global invariant topology, independent of local curvature, suggesting that the universal features of this programmable potential govern defect regulation.

Theoretical analysis.—To quest for the physical origin of regulated defects during DNACC crystallization on a curved surface, we derive an explicit expression for the effective potential combining entropic and enthalpic contributions. To this end, umbrella sampling method [52,53] is implemented to calculate the effective potential at different temperatures, as shown in Fig. 3(a). One sees that the potential is almost purely repulsive at a high temperature ($T^* = 2.0$). As T decreases, the potentials show a temperature-dependent, short-range attraction, whose strength increases monotonically with decreasing temperature. When two DNACCs approach each other, it is known they exert on each other effective repulsion due to the osmotic pressure arising between DNA chains from different colloids [54–56]. To quantify this purely entropic repulsion, the umbrella sampling simulations are technically performed by turning off the interaction between attractive sticky ends. As demonstrated by Fig. 3(b), the entropy change is T-independent and well captured by a truncated shifted Yukawa potential typical to the star polymer-like topology of DNACCs [57]:

$$\Delta S(r) = -k_B\gamma f^{\frac{3}{2}}\exp\left(\frac{-\alpha r}{\sigma}\right)\cdot\frac{\sigma}{r} - \left[(r-2r_1)\left(\frac{d\Delta S(r)}{dr}\right)_{r=2r_1} + \Delta S(2r_1)\right], \quad r \leqslant 2r_1. \tag{2}$$

The potential parameters are $\gamma = 17.7$ and $\alpha = 0.180$.

The difference between the two calculated effective potentials provides a measure of energy change afforded by the hybridization of sticky ends. Figure 3(c) demonstrates that less sticky ends can hybridize at higher temperatures due to thermal fluctuation, resulting in less energy change. Moreover, the variation of energy change with distance has the same tendency at all temperatures, suggesting a scaling form of ΔU as

$$\Delta U(r, T) = f(T)\cdot\Delta U_t(r). \tag{3}$$

Here, ΔU_t is the theoretical energy change if all sticky ends in the overlap region of neighboring DNACCs are bound, estimated by analyzing the effective space volume accessible to sticky ends that can bind to each other, as schemed by the inset of Fig. 3(a) [42]:

$$\Delta U_t(r) = -n_l f \epsilon_0 \frac{V_b^*}{V_f}. \tag{4}$$

Here, V_b^* and V_f are the effective volume of space accessible to bound sticky ends and volume of space accessible to free sticky ends, respectively. The form factor $f(T)$, of which the physical meaning is the fraction of bound sticky ends at equilibrium, is obtained by fitting Eq. (3), and the T dependence of form factor is well described by a two state expression [Fig. 3(d)] [58],

$$f(T) = \left[1 + \exp\left(\frac{\Delta U_0 - T\Delta S_0}{k_B T}\right)\right]^{-1}, \tag{5}$$

where $\Delta U_0 = -6.13\epsilon$ and $\Delta S_0 = -5.04 k_B$ measure, respectively, the energy and entropy change associated with the formation of hybridized sticky ends. The good agreement between the values of ΔU_0 and ϵ_0 corroborates again the validity of this theoretical model. Thus far, combining Eqs. (2)–(5), we have provided the detailed forms of the entropic and enthalpic components, leading to the explicit expression of the effective potential between DNACCs, as displayed by the lines in Fig. 3(a).

Discussion.—Essentially, the shape of this potential is quite different from other general potentials, such as Lennard-Jones potential or purely repulsive potentials, where the left-hand side of the potential well is the steeper one or gets more extreme at shorter distances. Fundamentally, this is attributable to the unique interplay between enthalpic and entropic contributions to the interaction potential of DNACCs [Fig. 3]. As demonstrated by Figs. 3(b) and 3(c) and the inset diagrams, the sharp transition on the right-hand side of the potential well is due to the bond stretching that can induce an extreme increase of the energy upon a small increase of the distance, in striking contrast to the negligible change of the entropic contribution. However, on the left-hand side of the potential well, the change of enthalpic contribution due to the bonds becomes much weaker while the entropic penalty originating from the reduced conformation of the compressed chains turns to be dominant, resulting in a relatively mild change of the potential. In comparison to the regular sixfold arrangement of DNACCs, a fivefold defect causes chain compression whereas a sevenfold defect leads to bond stretching [5]. Thus, the left-hand side of the potential well dominates the stability of the fivefold defect while the right-hand side governs that of the sevenfold defect.

Decreasing temperature regulates the shape of the potential well, leading to different changes on its both sides [Fig. 3(a)]. On the one hand, the slope of the right-hand side becomes remarkably steeper, making the sevenfold defects unstable. On the other hand, the convexity of the left-hand side changes from convex to concave. As illustrated in Fig. 4(a), for a regular fivefold defect, DNACCs are compelled to maintain closer to each other to uphold this particular configuration, where r should separate into diverse distances shorter than the equilibrium distance of the hexagonal arrangement r_{eq}, such as r_{s1} and r_{s2}. For the concave curve, there is an inflection point at $r_{ip} \lesssim r_{eq}$. In view of the theory of phase transition [59], when $r < r_{ip}$, the curvature of the effective potential is negative, and thereby, even tiny distance fluctuations lower the free energy, giving rise to the spontaneous separation of r, which facilitates the formation and stability of an isolated fivefold defect. In contrast, the second derivative remains positive for the convex curve, indicating that the separation of r becomes much harder as it requires large fluctuations. Altogether, the shape change of this potential will lead to the swap from scars consisting of five and sevenfold defect pairs to isolated fivefold defects when decreasing the temperature. In this case, the critical temperature of this swap occurs at around $T_c^* \approx 1.2$, as observed in Figs. 1(b) and 2(d). This is in good agreement with the analytical result $T_c^* = 1.18$, determined by the inflection point where the second derivative vanishes [Fig. 3(a)].

To consolidate the potential shape-dominated defect configurations, we conduct additional MD simulations, describing the pairwise colloid interactions by this theoretical effective potential, based on aforementioned methods. Moreover, standard NVT Monte Carlo (MC)

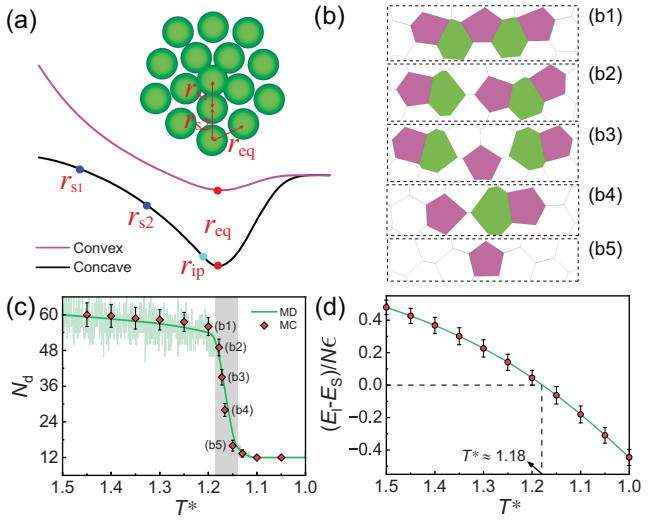

FIG. 4. (a) Schematic of the convexity of the effective potential and a regular fivefold disclination. (b) Snapshots of ground states at different T^* obtained in MC simulations, as indicated in (c). (c) N_d versus T^* for MD and MC simulations. (d) Energy difference per particle between isolated defects (E_I) and scars (E_S) as represented in (b5) and (b1), respectively.

simulations with the effective potential are performed to identify the ground states at different temperatures [55,60]. In MC simulations, each trial move is an attempted displacement of a random particle on the sphere, which is generated in a rotated reference frame to ensure the displacement is random and independent of the polar angle [61]. To ensure equilibration of the particles at high densities, at least 8×10^8 trial moves per particle are performed at a temperature [62]. Consistent with the flanking bead model, the results reproduce the sharp change of defect number around $T^* \approx 1.18$ [Fig. 4(c)] and definitely present the swap of the ground state from nonisolated to isolated defects upon cooling [Fig. 4(b)]. This is further corroborated by quantifying the energy difference between these two states, where the value changes from positive to negative around $T^* \approx 1.18$, rationalizing the swap of the defect configurations [Fig. 4(d)].

Conclusion.—We demonstrate that the interaction potential of DNACCs can be programmed to effectively control defects and even achieve perfect icosahedral order on a spherical surface. The unique shape of this potential determines the stability of different defect configurations, with the convexity of the left-hand side of the potential well governing the fivefold defect while the slope of the right-hand side dominates the sevenfold defect. We demonstrate how the potential can be shaped by varying the temperature to fine-tune the number as well as configuration of defects. The explicit analytic forms of entropic and enthalpic components of potential capture the numerical phenomenology and unravel its physical origins. The newly derived effective pair potential between DNACCs bears broad potential applications, not only in curved spaces but also for the ordering of DNACCs in standard flat geometries systems. Altogether, the study proposes a practical method to tune the disorder-order transitions on curved manifolds and might be of immediate interest to the design of novel configurations of colloidal crystals with controllable defects.

We thank Yan Xiong and Pengyu Chen for stimulating discussions. We acknowledge support from the National Natural Science Foundation of China (Grants No. 22025302, No. 22303029, and No. 21873053). L.-T. Y. acknowledges financial support from Ministry of Science and Technology of China (Grant No. 2022YFA1203203) and State Key Laboratory of Chemical Engineering (No. SKL-ChE-23T01). T. T. was supported by the Institute for Basic Science (IBS-R020-D1).

*Corresponding author: ltyan@mail.tsinghua.edu.cn

[1] D. L. D. Caspar and A. Klug, Cold Spring Harb. Symp Quant. Biol. **27**, 1 (1962).
[2] C. J. Marzec and L. A. Day, Biophys. J. **65**, 2559 (1993).
[3] H. W. Kroto, J. R. Heath, S. C. O'Brien, R. F. Curl, and R. E. Smalley, Nature (London) **318**, 162 (1985).
[4] A. R. Bausch, M. J. Bowick, A. Cacciuto, A. D. Dinsmore, M. F. Hsu, D. R. Nelson, M. G. Nikolaides, A. Travesset, and D. A. Weitz, Science **299**, 1716 (2003).
[5] W. T. M. Irvine, V. Vitelli, and P. M. Chaikin, Nature (London) **468**, 947 (2010).
[6] R. E. Guerra, C. P. Kelleher, A. D. Hollingsworth, and P. M. Chaikin, Nature (London) **554**, 346 (2018).
[7] P. Lipowsky, M. J. Bowick, J. H. Meinke, D. R. Nelson, and A. R. Bausch, Nat. Mater. **4**, 407 (2005).
[8] W. T. M. Irvine, M. J. Bowick, and P. M. Chaikin, Nat. Mater. **11**, 948 (2012).
[9] H. Kusumaatmaja and D. J. Wales, Phys. Rev. Lett. **110**, 165502 (2013).
[10] G. Meng, J. Paulose, D. R. Nelson, and V. N. Manoharan, Science **343**, 634 (2014).
[11] F. C. Frank and J. S. Kasper, Acta Crystallogr. **11**, 184 (1958).
[12] M. J. Bowick and L. Giomi, Adv. Phys. **58**, 449 (2009).
[13] T. Erber and G. M. Hockney, Adv. Chem. Phys. **98**, 495 (1997).
[14] M. J. Bowick, D. R. Nelson, and A. Travesset, Phys. Rev. B **62**, 8738 (2000).
[15] M. Bowick, A. Cacciuto, D. R. Nelson, and A. Travesset, Phys. Rev. Lett. **89**, 185502 (2002).
[16] A. Pérez-Garrido and M. A. Moore, Phys. Rev. B **60**, 15628 (1999).
[17] S. Schneider and G. Gompper, Europhys. Lett. **70**, 136 (2005).
[18] M. Zhong, R. Wang, K. Kawamoto, B. D. Olsen, and J. A. Johnson, Science **353**, 1264 (2016).
[19] G. Tarjus, F. Sausset, and P. Viot, Adv. Chem. Phys. **148**, 251 (2012).
[20] S. Angioletti-Uberti, B. M. Mognetti, and D. Frenkel, Phys. Chem. Chem. Phys. **18**, 6373 (2016).
[21] J. P. Straley, Phys. Rev. B **30**, 6592 (1984).
[22] J. Tobochnik and P. M. Chapin, J. Chem. Phys. **88**, 5824 (1988).
[23] S. Prestipino, M. Ferrario, and P. Giaquinta, Physica (Amsterdam) **187A**, 456 (1992).
[24] C. Negri, A. L. Sellerio, S. Zapperi, and M. C. Miguel, Proc. Natl. Acad. Sci. U.S.A. **112**, 14545 (2015).
[25] J. M. Caillol and D. Levesque, Phys. Rev. B **33**, 499 (1986).
[26] J. M. Caillol, J. Chem. Phys. **96**, 1455 (1992).
[27] S. Angioletti-Uberti, P. Varilly, B. M. Mognetti, and D. Frenkel, Phys. Rev. Lett. **113**, 128303 (2014).
[28] W. G. Hoover and F. H. Ree, J. Chem. Phys. **49**, 3609 (1968).
[29] C. A. Mirkin, R. L. Letsinger, R. C. Mucic, and J. J. Storhoff, Nature (London) **382**, 607 (1996).
[30] A. P. Alivisatos, K. P. Johnsson, X. Peng, T. E. Wilson, C. J. Loweth, M. P. Bruchez, and P. G. Schultz, Nature (London) **382**, 609 (1996).
[31] Y. Yin and A. P. Alivisatos, Nature (London) **437**, 664 (2005).
[32] E. V. Shevchenko, D. V. Talapin, N. A. Kotov, S. O'Brien, and C. B. Murray, Nature (London) **439**, 55 (2006).
[33] D. Nykypanchuk, M. Maye, D. van der Lelie, and O. Gang, Nature (London) **451**, 549 (2008).

[34] S. Y. Park, A. K. R. Lytton-Jean, S. Weigand, B. Lee, G. C. Schatz, and C. A. Mirkin, Nature (London) **451**, 553 (2008).
[35] A. Kuzyk, R. Schreiber, Z. Fan, G. Pardatscher, E.-M. Roller, A. Högele, F. C. Simmel, A. O. Govorov, and T. Liedl, Nature (London) **483**, 311 (2012).
[36] E. Auyeung, T. I. N. G. Li, A. J. Senesi, A. L. Schmucker, B. C. Pals, M. O. de la Cruz, and C. A. Mirkin, Nature (London) **505**, 73 (2014).
[37] A. V. Tkachenko, Phys. Rev. Lett. **89**, 148303 (2002).
[38] D. B. Lukatsky and D. Frenkel, Phys. Rev. Lett. **92**, 068302 (2004).
[39] R. Dreyfus, M. E. Leunissen, R. Sha, A. V. Tkachenko, N. C. Seeman, D. J. Pine, and P. M. Chaikin, Phys. Rev. Lett. **102**, 048301 (2009).
[40] S. Angioletti-Uberti, B. M. Mognetti, and D. Frenkel, Nat. Mater. **11**, 518 (2012).
[41] D. Joshi, D. Bargteil, A. Caciagli, J. Burelbach, Z. Xing, A. S. Nunes, D. E. Pinto, N. A. Araújo, J. Brujic, and E. Eiser, Sci. Adv. **2**, e1600881 (2016).
[42] See Supplemental Material at http://link.aps.org/supplemental/10.1103/PhysRevLett.132.048201 for details of simulation model and methods, calculation of the theoretical energy change, and umbrella sampling, which includes Refs. [43–45].
[43] M. P. Allen and G. Germano, Mol. Phys. **104**, 3225 (2006).
[44] A. Nikoubashman, D. A. Vega, K. Binder, and A. Milchev, Phys. Rev. Lett. **118**, 217803 (2017).
[45] Z. Zhang, M. A. Horsch, M. H. Lamm, and S. C. Glotzer, Nano Lett. **3**, 1341 (2003).
[46] C. Knorowski, S. Burleigh, and A. Travesset, Phys. Rev. Lett. **106**, 215501 (2011).
[47] T. I. N. G. Li, R. Sknepnek, and M. O. de la Cruz, J. Am. Chem. Soc. **135**, 8535 (2013).
[48] Q. Yu, X. Zhang, Y. Hu, Z. Zhang, and R. Wang, ACS Nano **10**, 7485 (2016).
[49] G. Zhu, Z. Xu, Y. Yang, X. Dai, and L.-T. Yan, ACS Nano **12**, 9467 (2018).
[50] A. Kumar and J. Bechhoefer, Nature (London) **584**, 64 (2020).
[51] H. Xiong, D. van der Lelie, and O. Gang, Phys. Rev. Lett. **102**, 015504 (2009).
[52] A. Cacciuto, S. Auer, and D. Frenkel, Nature (London) **428**, 404 (2004).
[53] J. Kästner and W. Thiel, J. Chem. Phys. **123**, 144104 (2005).
[54] C. N. Likos, H. Löwen, M. Watzlawek, B. Abbas, O. Jucknischke, J. Allgaier, and D. Richter, Phys. Rev. Lett. **80**, 4450 (1998).
[55] M. Camargo and C. N. Likos, Phys. Rev. Lett. **104**, 078301 (2010).
[56] F. Sciortino, Y. Zhang, O. Gang, and S. K. Kumar, ACS Nano **14**, 5628 (2020).
[57] T. A. Witten and P. A. Pincus, Macromolecules **19**, 2509 (1986).
[58] C. W. Hsu, F. Sciortino, and F. W. Starr, Phys. Rev. Lett. **105**, 055502 (2010).
[59] L. D. Landau and E. M. Lifshitz, *Statistical Physics* (Elsevier, New York, 2013).
[60] D. Frenkel and B. Smit, *Understanding Molecular Simulation: From Algorithms to Applications* (Academic Press, San Diego, 2023).
[61] A. Novikov, D. Kuzmin, and O. Ahmadi, Appl. Math. Comput. **364**, 124670 (2020).
[62] S. Auer and D. Frenkel, Nature (London) **413**, 711 (2001).